

# Cometary ion drift energy and temperature at comet 67P/Churyumov–Gerasimenko

Hayley N. Williamson<sup>1</sup>  <sup>1</sup>★, Annie Johansson,<sup>2</sup> Romain Canu-Blot,<sup>1,3</sup> Gabriella Stenberg Wieser<sup>1,3</sup> , Hans Nilsson<sup>1,3</sup> , Fredrik L. Johansson<sup>4</sup> and Anja Moeslinger<sup>1,3</sup> 

<sup>1</sup>Swedish Institute of Space Physics, SE-981 92 Kiruna, Sweden

<sup>2</sup>Department of Computer Science, Electrical and Space Engineering, Luleå University of Technology, SE-981 92 Kiruna, Sweden

<sup>3</sup>Department of Physics, Umeå University, SE-901 87 Umeå, Sweden

<sup>4</sup>ESA/ESTEC, Keplerlaan 1, 2201AZ Noordwijk, Netherlands

Accepted 2024 July 30. Received 2024 July 15; in original form 2024 March 7

## ABSTRACT

The Ion Composition Analyzer (ICA) on the *Rosetta* spacecraft observed both the solar wind and the cometary ionosphere around comet 67P/Churyumov–Gerasimenko for nearly two years. However, observations of low energy cometary ions were affected by a highly negative spacecraft potential, and the ICA ion density estimates were often much lower than plasma densities found by other instruments. Since the low energy cometary ions are often the highest density population in the plasma environment, it is nonetheless desirable to understand their properties. To do so, we select ICA data with densities comparable to those of *Rosetta*'s Langmuir Probe (LAP)/Mutual Impedance Probe (MIP) throughout the mission. We then correct the cometary ion energy distribution of each energy-angle scan for spacecraft potential and fit a drifting Maxwell–Boltzmann distribution, which gives an estimate of the drift energy and temperature for 3521 scans. The resulting drift energy is generally between 11–18 eV and the temperature between 0.5–1 eV. The drift energy shows good agreement with published ion flow speeds from LAP/MIP during the same time period and is much higher than the cometary neutral speed. We see additional higher energy cometary ions in the spectra closest to perihelion that would be well described by a second Maxwellian-like distribution. The energy and temperature are negatively correlated with heliocentric distance, with a stronger dependence on heliocentric distance for temperature. It cannot be quantitatively determined whether this trend is primarily due to heliocentric distance or spacecraft distance to the comet, which increased with decreasing heliocentric distance.

**Key words:** methods: data analysis – plasmas – space vehicles: instruments – comets: individual: 67P.

## 1 INTRODUCTION

The interaction of the solar wind with a comet has been observed at multiple comets, primarily flybys of comets 21P/Giacobini–Zimmer (e.g. Brandt et al. 1985), 1P/Halley (e.g. Gringauz et al. 1986), and 26P/Grigg–Skjellerup (e.g. Grensemann & Schwehm 1993). However, a better understanding of comet magnetospheres required long-term observations. Subsequently, the *Rosetta* mission, designed to rendezvous with and orbit a comet, was launched in 2004. It arrived at comet 67P/Churyumov–Gerasimenko on 2014 August 8 and orbited until 2016 September 30, when it was deorbited into the comet nucleus. While comet 67P was less active than the comets of previous flyby missions, *Rosetta*'s escort of the comet from 3.6 au to perihelion at 1.2 au and back out to 3.8 au offered the first opportunity to observe a changing comet. In particular, the plasma environment of comet 67P changed drastically with heliocentric distance, beginning with a solar wind-dominated environment that became increasingly cometary ion-dominated as higher insolation led to higher outgassing

rates (Nilsson et al. 2015, 2017). Neutral particles outgassed from the nucleus are subsequently ionized by photoionization and electron impact ionization. These newborn cometary ions radially expand from the nucleus and are accelerated by electric fields (Nilsson et al. 2018; Moeslinger et al. 2023a), to eventually be picked up by and mass load the solar wind (e.g. Szegő et al. 2000; Coates 2004).

The plasma environment around the comet is largely dominated by three different types of electric fields, all of which vary with both distance from the comet and comet distance from the sun. When ions are born from the neutral cometary atmosphere, they originally expand radially away from the nucleus. The electrons have a much higher thermal speed than the ions, creating a pressure gradient that leads to a charge separation and hence an ambipolar electric field. This ambipolar electric field accelerates the ions such that their flow velocity is significantly greater than that of the neutrals (Vigren & Eriksson 2017) and is strongest close to the comet nucleus (Deca et al. 2019). The ambipolar field magnitude is proportional to the electron number density gradient,  $\sim 1/r$  (Vigren & Eriksson 2017). Thus, ions are continuously accelerated as they travel radially outwards from the comet. Higher energy ions are therefore assumed to have been born further away from the spacecraft than lower energy ions.

\* E-mail: [hayley.williamson@irf.se](mailto:hayley.williamson@irf.se)

However, the ambipolar field is not the only electric field the cometary ions experience. Because of the small size of the comet ionosphere and weak interplanetary magnetic field strength, the ion gyroradius (particularly for the cometary ions) is much larger than the ionosphere size, even close to perihelion, making them essentially unmagnetized (Williamson et al. 2022). However, electrons have a much smaller gyroradius and as such experience  $\vec{E} \times \vec{B}$  drift. The different motions of the ions and electrons thus create a polarization electric field in an anti-sunward direction. The polarization electric field is strongest at intermediate heliocentric distances: low-column densities far from perihelion will cause a small electric field magnitude, while at high column densities near perihelion, the cometary ionosphere modifies the solar wind electric field significantly enough that the ionosphere does not experience the tailward electric field (Nilsson et al. 2018). Eventually, at the furthest distances from the nucleus, the ions are picked up by the solar wind convective electric field and begin to gyrate in the interplanetary magnetic field. Both low-energy newborn ions, in the process of being accelerated by the ambipolar electric field, and higher energy pickup ions were observed by *Rosetta* at comet 67P (Nicolaou et al. 2017; Nilsson et al. 2017; Stenberg Wieser et al. 2017; Berčič et al. 2018; Masunaga et al. 2019).

While *Rosetta* orbited relatively close to the comet nucleus, the expansion of the comet magnetosphere with decreasing heliocentric distance allowed for measurements of various solar wind-cometary ion interaction regions (Williamson et al. 2020). Near perihelion, the cometary magnetosphere was extensive enough to exclude the solar wind entirely, creating a region called the solar wind ion cavity, and at times even exclude the interplanetary magnetic field, forming a diamagnetic cavity (Goetz et al. 2016a,b). The time period where the cometary ionosphere reaches a comparable pressure to the solar wind and as such is able to significantly deflect the solar wind is of particular interest, as it indicates a fully formed induced magnetosphere. Observations just outside of the solar wind ion cavity, where cometary ion momentum flux is greater than the solar wind momentum flux, are analogous to those near an induced magnetospheric boundary at an unmagnetized planet, where the plasma transitions from solar wind dominated to planetary ion dominated. Thus, this boundary is often referred to as a cometopause (e.g. Mandt et al. 2016). Solar wind ion distributions during this time are similar to those found in a magnetosheath, suggesting the presence of a bow shock (Williamson et al. 2022). This highly dynamic region is likely to have formed various types of plasma instabilities (e.g. Kelvin–Helmholtz instabilities seen at Venus and Mars, Wolff, Goldstein & Yeates 1980; Ruhunusiri et al. 2016; Poh et al. 2021); however, thorough knowledge of the plasma pressure tensor is useful for analysis of such instabilities. Thus far, such analysis has been complicated by incomplete knowledge of ion temperatures at comet 67P due to instrumental effects, as described below.

*Rosetta* routinely experienced highly negative spacecraft potential ( $V_{s/c}$ ), sometimes exceeding  $-15$  V (Odelstad et al. 2015, 2017), a result of exposed positively charged connectors on the large solar panels (Johansson et al. 2020). The negative spacecraft charging has the effect of repelling electrons and attracting lower energy positive ions. This affects plasma measurements, such as those made by the Ion Composition Analyzer (ICA) (Nilsson et al. 2007), part of the *Rosetta* Plasma Consortium (Carr et al. 2007). ICA was designed to study the interaction between the solar wind and cometary ions by measuring positive ions through a wide range of energies and masses. As such, it is capable of measuring the low-energy ions that contribute the bulk of the pressure close to perihelion. However, the spacecraft

potential both accelerates and distorts the trajectories of these ions, changing their energy distribution. This has the largest effect on ions with energies  $\lesssim |2V_{s/c}|$  (Bergman et al. 2020a, 2021a,b). In addition, ion densities measured by ICA were often much lower than those measured by the RPC Langmuir Probe (LAP) (Eriksson et al. 2007) and Mutual Impedance Probe (MIP) (Trotignon et al. 2007). It is unclear why this is the case, as the ICA densities can be up to two orders of magnitude lower than those found by LAP/MIP. One likely possibility is that the distortion of low energy ion trajectories by the spacecraft potential, combined with the limited ICA field of view, prevents ICA from measuring the full cometary ion distribution. If too few low-energy ions are measured, a distribution cannot be inferred, and so no temperature can be calculated. Thus, finding the temperature necessary for the thermal pressure requires data with a reasonably complete distribution.

Here, we select ICA data that contain a low energy cometary ion distribution representative of the surrounding plasma by selecting time periods with densities comparable to that of LAP/MIP and correct the data for the spacecraft potential. The resulting distribution is then fit to find both the drift energy and temperature of the cometary ions across a wide span of the comet’s orbit, allowing us to draw conclusions on how both parameters change with heliocentric distance. This can then be used in future work to help calculate the ion thermal pressure, while also giving insight into the changing distributions of the cometary ions.

## 2 INSTRUMENT DESCRIPTION

In this work, we use data from three instruments in the *Rosetta* Plasma Consortium (RPC): the Ion Composition Analyzer (ICA), the Langmuir Probe (LAP), and the Mutual Impedance Probe (MIP). The bulk of the data used is from ICA, with cross-calibrated LAP–MIP data used for ICA data selection and spacecraft potential.

### 2.1 Ion composition analyzer

The Ion Composition Analyzer (ICA) (Nilsson et al. 2007) was an ion mass spectrometer in the *Rosetta* Plasma Consortium (RPC) package (Carr et al. 2007). The instrument design consisted of an electrostatic entrance deflection system, used to determine ion arrival angle, a hemispherical electrostatic analyzer for energy analysis, a magnetic mass analyzer, and a microchannel plate detector. ICA measured ions in the energy range of a few eV  $q^{-1}$  to 40 keV  $q^{-1}$  in 96 energy steps, with  $\Delta E/E = 0.07$  for  $E > 30$ eV and 0.30 for  $E < 30$ eV, and had a mass resolution of  $M/\Delta M \sim 2$ . This mass resolution can distinguish between masses 1, 2, 4, 8, 16, and 32 amu  $q^{-1}$ . In this paper, we treat all ions with masses  $> 16$  amu  $q^{-1}$  as water group ions originating from the comet. Each full energy-angle scan took 192 s.

ICA had a nominal angular field of view of  $2\pi$  sr, with  $90^\circ \times 360^\circ$  coverage with a resolution of  $5.625^\circ \times 22.5^\circ$  in elevation and azimuth respectively, although a portion of this field of view is in practice blocked by the spacecraft. However, this field of view is not applicable to the lowest energy ions, such as those discussed here. Elevation bins are sampled using electrostatic deflection. Thus, the elevation range is dependent on the energy bin being measured, and so for low energies ( $\lesssim 100$ eV), only the central elevation bins are scanned over due to difficulties in setting deflector voltages accurately. This makes the viewing direction energy dependent, such that the elevation range decreases with energy until only the centre elevation bin is scanned for the lowest energy-elevation setting (Nilsson 2021b). Additionally, the negative spacecraft potential

highly distorts ion trajectories at these energies (Bergman et al. 2020a). As such, all data used in this study were summed over all angular directions to produce a 1D distribution in energy. For the spectra, we use the heavy ion data from the ‘HVY.TAB’ files in the level 4 mass-separated Phys-Mass data set in the ESA Planetary Science Archive (Nilsson 2021a).

### 2.1.1 Energy table correction

For an electrostatic analyzer such as that used in ICA, only a small subset of ions will pass through the entire analyzer depending on their energy and the voltages applied to the electrodes of the ESA. Thus, in order to understand the energy of the arriving ions, the instrument must have a table of voltages to apply to the ESA which are then converted to an energy passband. This conversion is then the instrument energy table. The ICA energy table required updating upon arrival at comet 67P, when it was discovered that the ICA high voltage system had an offset compared to on-ground calibration results (Nilsson et al. 2017). After update, the uncertainty in ion energies is roughly 3 eV. However, there is an additional high voltage drift related to the instrument temperature, which occurs when ICA cooled to below 13.5°C. This can be corrected with the formula:

$$E_c = \begin{cases} E_0 + (13.5 - T_s) \times 0.7 & \text{if } T_s < 13.5^\circ\text{C} \\ E_0 & \text{otherwise} \end{cases} \quad (1)$$

where  $E_c$  is the corrected energy,  $T_s$  is the sensor temperature, and  $E_0$  is the original energy. This formula has been applied to all data used in this study.

## 2.2 Langmuir probe and mutual impedance probe

The *Rosetta* Plasma Consortium also contained a Langmuir probe instrument, LAP (Eriksson et al. 2007), and a Mutual Impedance Probe, MIP (Trotignon et al. 2007). Data from these two instruments provided spacecraft potential and electron density for this study, which were compared to the ICA ion density. LAP consisted of two spherical Langmuir probes, called LAP1 and LAP2, located on two booms mounted to the spacecraft. The boom lengths were 2.2 and 1.6 m for LAP1 and LAP2, respectively. The booms were positioned such that at least one of the probes was always sunlit and capable of measuring a radial outflow from the comet (Edberg et al. 2015). LAP primarily measured the current to the probes as a function of bias voltage, which can then be used to calculate plasma parameters such as spacecraft potential, electron density, and ion flow speed.

The Mutual Impedance Probe had two pairs of receiving and transmitting electrodes mounted to the LAP1 boom 1 m apart. MIP then could retrieve the plasma density by finding the plasma resonance frequency. If densities were low, MIP could also use the LAP2 probe as a transmitting electrode, thus increasing the baseline to 4 m. MIP density retrievals, unlike LAP, are independent of electron temperature (as long as the plasma frequency is within its measurement range) and not sensitive to the spacecraft potential, as was found later (Wattiaux et al. 2020; Bucciattini et al. 2023). Thus, because the two measurement techniques are so different, they have been cross-calibrated to ensure high accuracy (Johansson et al. 2021). This cross-calibrated data set has been used in this study for the electron densities shown in Fig. 1 (‘ASW.TAB’ files) and spacecraft potential (‘USC.TAB’ files) (Eriksson et al. 2020). We additionally use the derived LAP ion speeds from the data set’s ‘ASW.TAB’ files for comparison with our fit parameters. The effective ion speed (i.e. a combination of the thermal and drift speeds) can be calculated

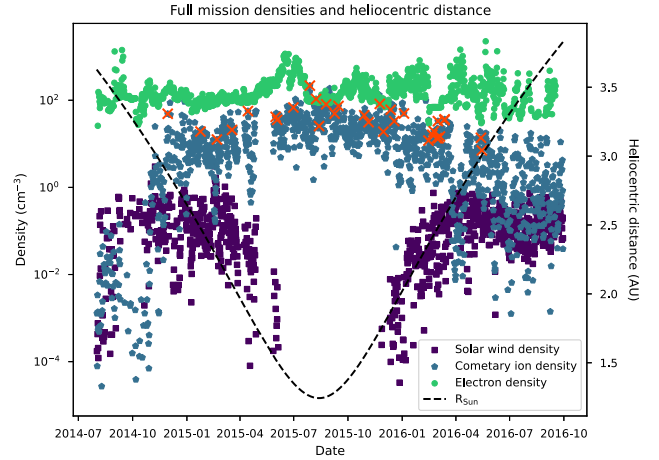


**Figure 1.** Electron (green circles), cometary ion (blue stars), and solar wind (purple squares) densities, averaged over 12 h, for the entire *Rosetta* mission. Electron densities are from the LAP/MIP cross-calibrated data and cometary and solar wind ion densities are from ICA. The black dashed line shows heliocentric distance. The orange crosses mark the 32 randomly chosen time periods for fitting.

from the ion current slope of the LAP bias voltage sweep using the equation:

$$\frac{dI}{dV} = \frac{q^2 n_i A_{LAP}}{2m_i u_i} \quad (2)$$

where  $dI/dV$  is the slope of the ion current region,  $q$  is the ion charge (assumed to be singly charged),  $n_i$  the plasma density from MIP,  $A_{LAP}$  is the surface area of the Langmuir probe,  $m_i$  the ion mass (assumed to be 19 in the LAP data set), and  $u_i$  is the effective ion speed (Vigren et al. 2017).

## 3 METHODS

### 3.1 Data selection

We use a few criteria to select ICA data that are both inside the cometopause, e.g. where the cometary ions are the dominant ion species but the solar wind can still be present (Mandt et al. 2016), and include most of the low energy ion distribution. First, we average the solar wind, cometary ion, and electron densities and pressures for every 12 h, approximately the rotation period of the comet, to smooth out variations from asymmetric outgassing. To ensure the data is inside the cometopause, we select only data where the cometary ion momentum flux is larger than the solar wind momentum flux (calculated as in Williamson et al. 2020). ICA ion densities are routinely lower than LAP/MIP electron densities, assumed to be due to unobserved low-energy ions. Selecting ICA data where the cometary ions are a significant percentage of the electron densities should help to mitigate the issue of the missing ions. We found that setting a threshold of  $n_c \geq 0.15n_e$  where  $n_c$  is the cometary ion density and  $n_e$  is the LAP/MIP electron density allowed for both a significant number of time periods that meet the condition as well as ensure ICA was observing the majority of the local plasma distribution.

Applying both of these conditions to the ICA data results in 259 12-h time periods suitable for analysis, 148 of which are in the solar wind ion cavity. We then take a random sample of 32 of the 259 time periods for use in the fitting procedure, giving 4676 suitable ICA scans to fit, as ICA was not on for the entirety of every 12 h period.

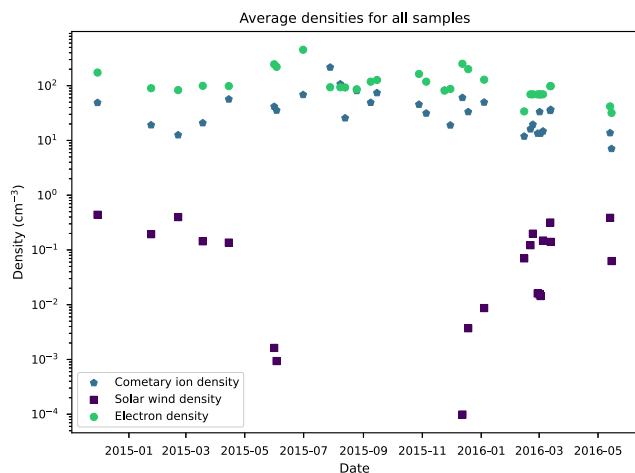


**Figure 2.** LAP/MIP electron (green circles), ICA cometary ion (blue stars), and ICA solar wind (purple squares) densities, averaged over 12 h, for the 32 chosen time periods. The ICA ion densities are the first order density moment.

Fig. 1 shows the 12-h averaged electron, cometary ion, and solar wind densities, as well as heliocentric distance, for the entirety of the main Rosetta mission, from 2014 August to 2016 September. The solar wind ion cavity is clearly visible as a gap around perihelion where the solar wind densities are non-existent, and times when *Rosetta* was inside the cometopause are roughly a few months on either side of the solar wind ion cavity. We show the 12-h time periods selected for fitting with orange X markers.

The densities of the 32 time periods are also shown in Fig. 2. We note that, even though our conditions ensure they are all inside the cometopause, the time periods still cover a wide range of conditions, with the local solar wind density varying by several orders of magnitude. 11 of the time periods are fully inside the solar wind ion cavity, with solar wind densities equal to zero, while the other 21 have both cometary and solar wind ions present. The comparison between the cometary ion densities and electron densities, showing that they are of a similar order of magnitude, can be seen in this figure.

### 3.2 Fitting method

To determine the bulk speed (drift energy) and 1D temperature of the low-energy ions, we fit a drifting Maxwell–Boltzmann distribution to the data. The same model was used previously in Bergman et al. (2021a) and Moeslinger et al. (2023b). The fit is done in energy space and the fit function is given by

$$f_E(E) = n \sqrt{\frac{1}{\pi k T_i E_i}} \exp\left(-\frac{E + E_i}{k T_i}\right) \sinh\left(\frac{2\sqrt{E E_i}}{k T_i}\right) \quad (3)$$

where  $n$  is the ion density,  $k$  the Boltzmann constant and hence  $k T_i$  is the ion temperature in eV, and  $E_i = m_i v_i^2/2$  is the ion drift energy, equivalent to the bulk speed in energy space. The full derivation of this equation can be found in appendix B of Bergman et al. (2021a). For some scans, the energy distribution has two peaks. For these cases, both peaks are fit with a two-peak version of equation (3) where the total fit is a sum of the fits for each peak. As will be shown in Section 4, some scan distributions have an additional higher energy tail, corresponding to pickup ions. These tails would be best fit with a kappa distribution; however, here, we choose to focus only on the low energy Maxwellian peaks, as these ions comprise the bulk of the plasma. Indeed, the value of the distribution function at low

energies is several orders of magnitude higher than that of higher energies, meaning the kappa distribution tail contributes little to the bulk plasma properties.

The Maxwellian model fit to the data from each scan is inspected manually and discarded if the fit quality is poor. We additionally calculate a modified index of agreement (Legates & McCabe 1999) for each fit to confirm the fit quality. Slightly less than 25 per cent of the 4676 scans could not be fit successfully, leaving 3521 scans from the 32 time periods shown in Fig. 2 with good quality fits, meaning that the fitted curve passes through the data points that compose the low energy Maxwellian peak, capturing both the peak location and width.

### 3.3 Spacecraft potential correction

As described in Section 1, spacecraft potential affects ions with energies roughly  $< |2V_{s/c}|$ . As we are interested in the low energy newborn cometary ions for this work, we must correct for the acceleration due to spacecraft potential. While Bergman et al. (2020a, 2020b) show that the spacecraft potential distorts the incoming direction of the low-energy ions, only the one dimensional energy distribution is needed to obtain bulk speed and temperature for this population. While in general a drifting Maxwellian cannot be distinguished from e.g. a symmetric ring or shell distribution in a 1D energy distribution, these low energy cometary ions have not been picked up and so will not have these distributions. As a result, we can safely assume the drifting Maxwellian fit in 1D is sufficient. Thus, when correcting for the effect of the spacecraft potential, we only correct for the energy added to the positive ions. This is done simply by adding the average (negative) spacecraft potential to the corresponding ICA ion energies. This method was confirmed with modelling in Bergman et al. (2021a). The new ion energies per charge in the energy distribution function will then be:

$$\frac{E_{\text{new}}}{q} = -V_{s/c} + \frac{E_{\text{ICA}}}{q} \quad (4)$$

where  $q$  is the ion charge (assumed to be one for the cometary ions) and  $E_{\text{new}}$  then replaces  $E$  in equation (3). An example where a drifting Maxwell–Boltzmann distribution has been fit to the data as described in Section 3.2 is shown in Fig. 3. For this sample, the mean spacecraft potential was  $-13.7$  V. The original data is shown in purple, with stars marking the measurements, while the data corrected for spacecraft potential are shown in blue, with X's marking the measurements. In the figure, it is evident that accounting for the spacecraft potential not only changes the peak energy as expected, but also changes the fitted temperature. The peak energy is always decreased and the temperature increased after the spacecraft potential correction, since the negative spacecraft potential both accelerates and adiabatically cools the ions. For our data set, the spacecraft potential estimate from LAP is generally between  $-20$  and  $-5$  V.

## 4 RESULTS

### 4.1 Fit examples

An example of a simple one peak fit is shown in Fig. 3 and panel (c) of Fig. 4. A higher energy tail not fit by the drifting Maxwell–Boltzmann function can be seen in Fig. 3; however, the distribution function is typically several orders of magnitude lower than that of the data fit by the function. Many scans, particularly closer to perihelion, contain more prominent high-energy tails that appear to fit an exponential or kappa distribution such as that in panel (a) of Fig. 4; we leave

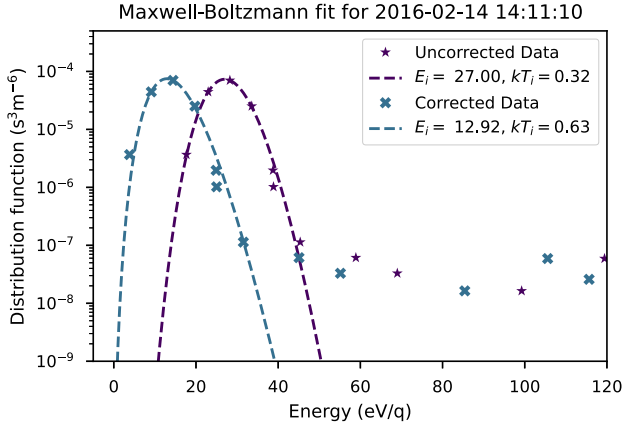


**Figure 3.** A single ICA scan from 2016 February 14 fit with a drifting Maxwell–Boltzmann distribution. Energy per charge in eV is shown on the  $x$ -axis and distribution function ( $\text{s}^3\text{m}^{-6}$ ) on the  $y$ -axis. The original, uncorrected ICA data and corresponding fit are shown in purple stars, while the data corrected for a spacecraft potential of  $-13.7\text{V}$  is shown in blue crosses. Resulting fit parameters are shown in the legend.

the study of these distributions to a future work. Other scans include a second clearly Maxwellian peak of smaller magnitude at higher energies. An example of this is shown in panel (b) of Fig. 4. As these form a minority of the scans, we only include the lower energy peak in our analysis. This second peak is a minor contribution to the total distribution, as it always has a lower amplitude than the primary low energy peak, but we nonetheless fit the second peak when it appears to ensure the correct fit for the lower energy peak.

As mentioned previously, approximately 25 per cent of the scans were unable to be successfully fit. This was primarily due to two reasons: either the distribution lacked a low-energy peak, or there was not enough data for fitting. Particularly close to perihelion, scans could have a broad, highly asymmetric distribution that could not be fit with the drifting Maxwell–Boltzmann, as they did not have a distinct peak. In other samples, scans occasionally lack a low-energy peak entirely, indicating ICA likely did not observe the full cometary ion distribution in that scan. We also set the requirement that a scan must have at least 5 data points in order to be fit, and that the resulting parameters must have  $E_i > 4\text{eV}$  and  $kT_i > 0.35\text{eV}$  as arbitrary lower limits to approximate the lowest values resolvable by the instrument based on examination of the data. The temperature lower limit was the result of the instrument energy resolution and the energy lower limit ensured there were measurements below the peak for a better fit. Scans excluded for this reason tended to be the samples farthest from perihelion, later in the mission. Thus, the ratio of skipped scans to total scans in a 12-h sample as a function of heliocentric distance has two peaks, with one peak close to perihelion from the unsuitable distributions and the second far from perihelion due to either an unresolvable distribution or too few data points.

#### 4.2 Parameters from all fits

In Fig. 5, we show the resulting fit parameters, drift energy (bulk velocity), and temperature, for all successful fits, with colour indicating heliocentric distance in au. Broadly, while there is a significant amount of scatter, there is also a relatively small range of values that contain most of the data, visible in the histogram in Fig. 6. 50 per cent of the data has drift energies between 11 and 18 eV (approximately  $11\text{--}14\text{ km s}^{-1}$  flow speed assuming  $\text{H}_2\text{O}^+$ ) and temperatures between

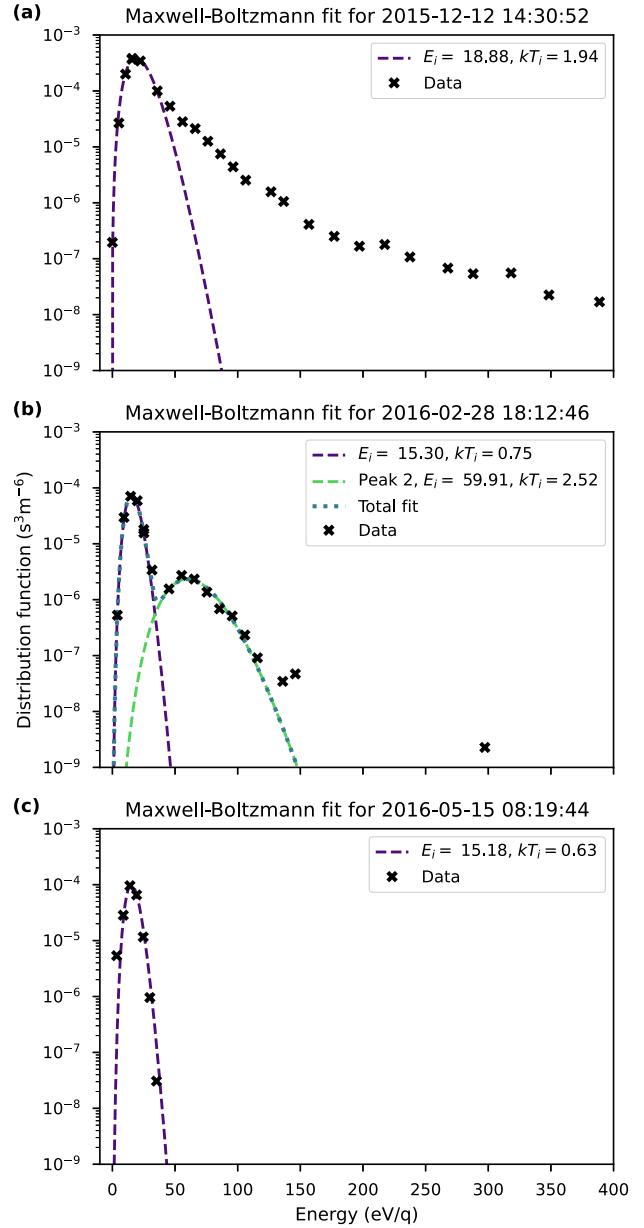


**Figure 4.** Examples of the three most typical energy distributions in the samples. Energy per charge in eV is shown on the  $x$ -axis and distribution function ( $\text{s}^3\text{m}^{-6}$ ) on the  $y$ -axis. Data is given in black crosses and the fits as a dashed purple line. Panel (a) shows a fit with one low-energy peak followed by a high-energy tail, panel (b) shows a distribution with two Maxwell–Boltzmann peaks, with the additional second peak fit in green dashed line and the total fit in blue dotted line, and panel (c) shows a single low-energy peak. The panels are ordered by increasing heliocentric distance.

0.5 and 1 eV. Both  $E_i$  and  $kT_i$  are lognormally distributed across the whole data set (not shown), with their individual distributions shown in the top and right panels of Fig. 6. The individual histograms for  $E_i$  and  $kT_i$  indicate that the lower limit cutoffs of 4 and 0.35 eV respectively do not drastically bias the data, as both show peaks well above the cutoff values.

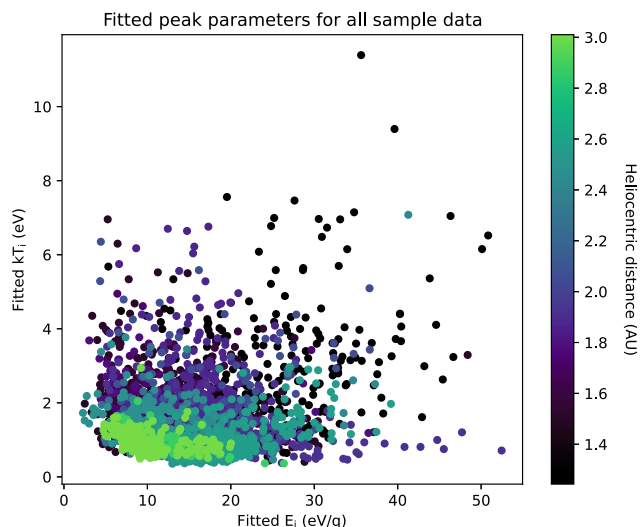


**Figure 5.** The peak drift energy ( $x$ -axis) and temperature ( $y$ -axis) for all 3521 scans with a successful fit. If a scan distribution included more than one peak, we have taken the energy and temperature of the lowest energy peak. Colour indicates heliocentric distance, as shown by the colourbar on the right.

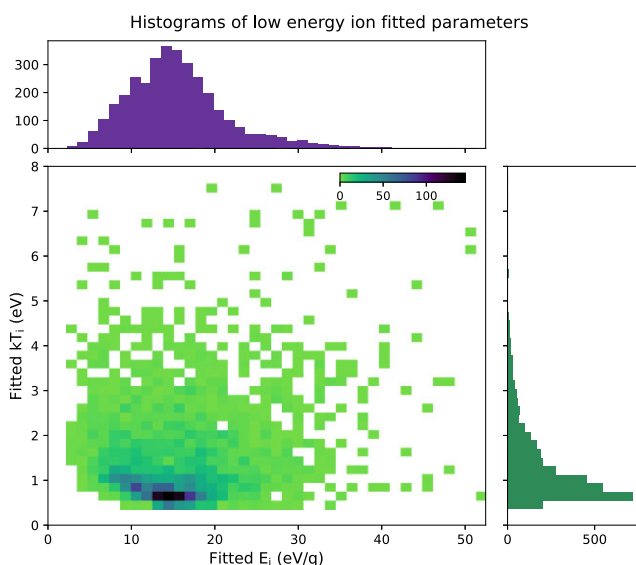


**Figure 6.** A histogram of all the fitted peak drift energy and temperature shown in Fig. 5. The top panel shows a histogram of the energy in purple, the middle shows a 2D histogram of both energy and temperature, and the right panel shows temperature in green.

### 4.3 Variations with heliocentric distance

One area of interest is the variation of the drift energy and temperature with heliocentric distance, as this controls the size and complexity of the comet environment. Additionally, finding such a trend would allow for generalization across the broader ICA data set. However, determining the effect of heliocentric distance is complicated by the varying spacecraft distance to the comet, which increased with decreasing heliocentric distance. The cometocentric distance in our data set thus ranged from a maximum of 397 km at a heliocentric distance of 1.25 au to a minimum of 9.5 km at 3 au. The increase on spacecraft cometocentric distance near perihelion was an effect of the increasing comet activity; the spacecraft endeavoured to remain as close to the nucleus as was possible to avoid large

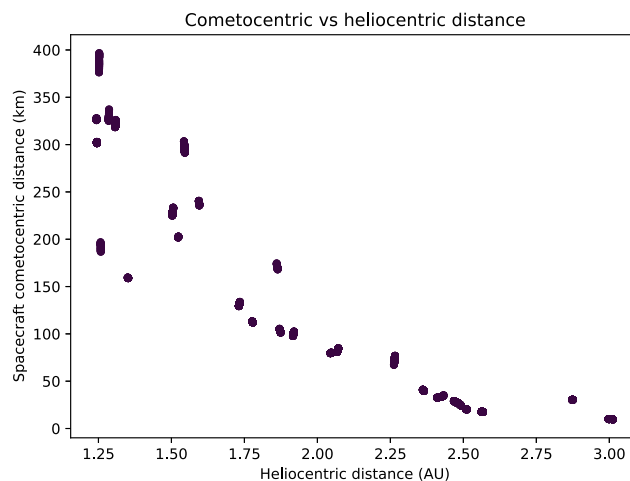


**Figure 7.** The distance from the comet to the Sun in au versus the spacecraft distance to the comet in km for all the data used in this study.

numbers of dust grains overwhelming the star trackers. For the plasma instruments, this had the effect of keeping the spacecraft in roughly the same plasma density corridor. In theory, the changing spacecraft distance should also affect the ion distributions observed by *Rosetta*, and so it would be desirable to disentangle the two effects.

Fig. 7 shows the strong correlation between heliocentric distance,  $R_{\text{sun}}$ , and cometocentric distance,  $r_{\text{com}}$ . The data examined for this study, while covering a wide portion of the *Rosetta* mission, simply do not cover enough parameter space where one distance varies much more than the other in order to fully disentangle the two effects. Therefore, here, we only show trends with respect to heliocentric distance, with discussion on the cometocentric dependence.

To ascertain trends in the data, we analyse the data sets using the Mann–Kendall test (Mann 1945; Kendall 1975; Gilbert 1987) and Theil–Sen regression (Sen 1968; Theil 1992). The Mann–Kendall test is a non-parametric test for monotonic trends. To assess the significance of the trend in the ICA data, we employed bootstrapping to determine the statistical distribution of the Mann–Kendall test under the null hypothesis of no trend. This involved repeated random sampling with replacement from the original data set. The significance of the trend is indicated by the observed positive or negative deviation of the Mann–Kendall test result (of the observed data) from the null-hypothesis distribution. The test is two-tailed, meaning it is capable of determining the presence of both positive and negative trends. We evaluate the test at a 95 per cent confidence level. We use a Theil–Sen regression to estimate the parameter trends in log space, resulting in a power law trend. Theil–Sen regression was chosen because it is a non-parametric method, and therefore no assumptions about the distribution of the data are required. Additionally, it is less sensitive to outliers than a traditional least-squares regression, which is useful for our data set.

From Fig. 5, it appears that there is more scatter, and hence, a larger scan-to-scan variation, in drift energy and temperature for lower heliocentric distances (darker colours). To test this hypothesis, we calculate the interquartile range of the variation for each sample period and validate the trend using the Mann–Kendall statistical test. The interquartile range, shown by the light coloured bands in Fig. 8, shows a significant decreasing trend with heliocentric distance for both  $E_i$  and  $kT_i$ . Thus, the plasma does indeed vary more from scan

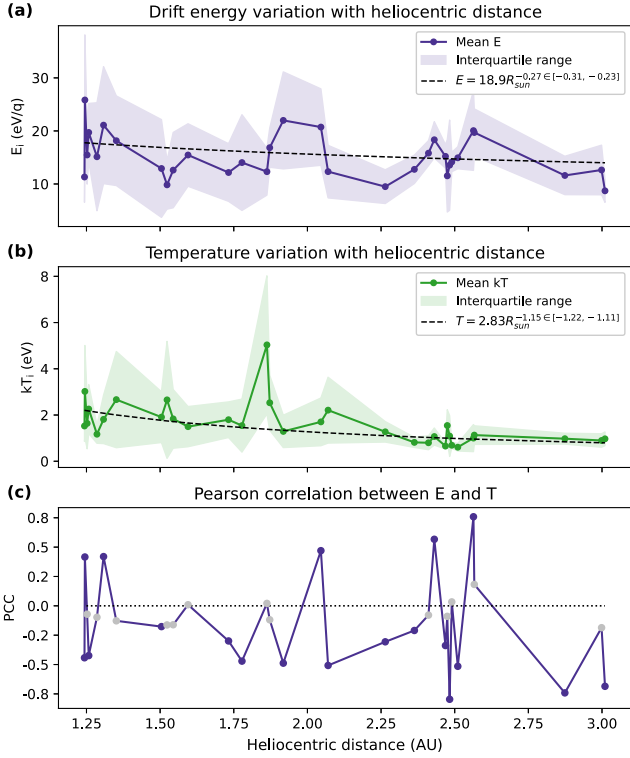


**Figure 8.** Variations of the fitted parameters with heliocentric distance in au. Panel (a) shows the mean drift energy per sample (eV) in dark purple dots, the interquartile range (25–75 per cent) for a sample in surrounding light purple, and the Theil–Sen power-law fit as a black dashed line. Panel (b) shows the same for temperature (eV) in green. The Theil–Sen regressions are given in the panel legends with the 95 per cent confidence intervals for the exponents. Panel (c) shows the Pearson correlation coefficient between E and T for each sample, with a dotted line indicating 0. Gray markers indicate a correlation coefficient with a p-value above 0.05 and are not statistically significant.

to scan at lower heliocentric distances, indicating a more dynamic plasma near perihelion.

We additionally use the Mann–Kendall test to investigate if the drift energy and temperature decrease with increasing heliocentric distance, followed by Theil–Sen regression to estimate a power law. While Fig. 8 shows the mean parameters per 12-h sample to minimize clutter, both the Mann–Kendall significance test and Theil–Sen estimate were done using the full data set. Both drift energy and temperature have a highly significant decreasing trend with increasing heliocentric distance. The decrease is small for energy, with the Theil–Sen regression giving trends of  $E = 18.85 R_{sun}^{-0.27}$ . However, for temperature the trend is noticeable, with the result  $T = 2.83 R_{sun}^{-1.15}$  with  $R_{sun}$  in au for both. Thus, while distance from the Sun does have a statistically significant effect on the low energy ion distributions, it has a much stronger effect on temperature than energy, which is approximately inversely proportional to heliocentric distance. To ensure this trend was not due to a change in the spacecraft potential, we also examined the spacecraft potential as a function of both distances and found no significant trend for our data set.

There is no overall strong correlation between  $E_i$  and  $kT_i$  in the full data set, although this is not always the case for individual 12 h samples. As seen in panel (c) of Fig. 8, many of the samples have a negative correlation, i.e.  $kT_i$  decreases as  $E_i$  increases. However, there are five samples with a statistically significant positive correlation, and other samples with no significant correlation at all. It is unclear

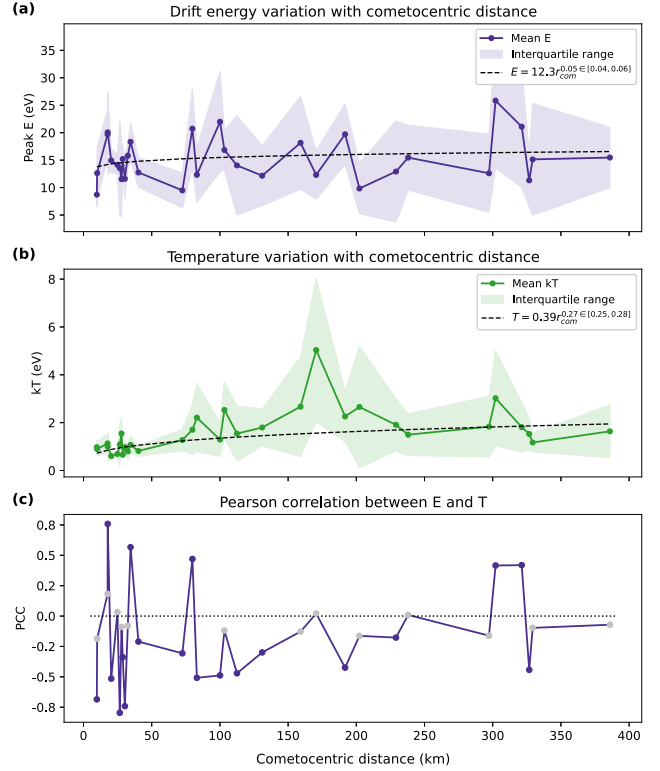


**Figure 9.** Variations of the fitted parameters with cometocentric distance in km. All panels are the same as in Fig. 8.

why both positive and negative correlations appear, and the type of correlation does not appear to relate to heliocentric distance. Possible causes of these varying correlations will be explored in Section 5.

Unsurprisingly, given the negative correlation between  $R_{sun}$  and  $r_{com}$ , the drift energy and temperature do show a positive correlation with cometocentric distance, shown in Fig. 9 with the same format as Fig. 8. As with the previous figure, only the mean values for each sample are plotted, but the Theil–Sen regression and the Mann–Kendall trend and significance were calculated using the full data set. Both energy and temperature have a statistically significant increasing trend with cometocentric distance, with results of  $E = 12.3 r_{com}^{0.05}$  for energy and  $T = 0.39 r_{com}^{0.27}$  for temperature, with  $r_{com}$  in km. While the significance of this correlation is similar to those for heliocentric distance, it is highly dependent on the subset of data chosen. For example, the temperature no longer shows any trend with cometocentric distance if only data with  $R_{sun} < 1.6$  au (which equates to  $r_{com} > 170$  km) are selected for the Theil–Sen regression. Even so, attempting to separate the effects of heliocentric versus cometocentric distance by choosing portions of data does not remove the inherent bias in the data set, as the two distances are much more strongly correlated with each other than with either fit parameter. With the data used in this study, it is therefore not possible to determine which distance has a stronger effect on the energy and temperature, although the correlation with heliocentric distance remains even if a subset of the data is chosen and the exponents of the trends are larger for both parameters, indicating a potentially stronger dependence. The relative importance of heliocentric versus cometocentric distance in the trends in energy and temperature are discussed below.

#### 4.4 Sensitivity to LAP potential

Previous comparisons of the spacecraft potential measured by LAP and the minimum energy of ions measured by ICA in Odelstad et al. (2017) show that neither measurement is necessarily a perfect indication of the true plasma potential. By comparing data from cases with a strong correlation between ICA and LAP, LAP was found to measure between 0.7–1 times the ‘true’ potential, with the fraction varying widely (cf. fig. 10 in Odelstad et al. 2017). To test the sensitivity of our results to the possibility of LAP measuring a fraction of the potential, we took a subset of eight samples evenly spaced in heliocentric distance. We refit the ICA spectra in these eight samples with the spacecraft potential scaled by a factor of 1.1, 1.2, 1.3, and 1.4 (corresponding to the fraction of potential measured) and reanalysed the results.

In general, this analysis showed that scaling the potential often shifted the minimum observed energy of the ion spectra to near or below zero, with the resulting drift energy fit parameter being much smaller than 1 eV. This was least evident for a factor of 1.1 (i.e. LAP measured  $0.9V_{s/c}$ ) and most evident for 1.4 (i.e. LAP measured  $0.7V_{s/c}$ ). Temperatures were shifted slightly higher, but the mean for  $1.4V_{LAP}$  was less than 0.2 eV higher than that for the original data set. The energy showed a stronger dependence on the potential scaling, with the mean energy decreasing from an original value of 13.4 eV for the eight samples to 9.6 eV for  $1.4V_{LAP}$ . So the average drift energy could, at maximum, decrease by a few eV. However, because  $1.4V_{LAP}$  often shifted the measured ion energies to nonphysical values, the difference is unlikely to be this large. The wide range of energies covered by the full data set regardless indicates the varying fraction of the potential LAP measures would not particularly change our results.

We additionally investigated the effect of the scaled potential on the heliocentric and cometocentric distance trends. The temperature shows essentially no change in the resulting Theil–Sen regression for either heliocentric or cometocentric distance. For energy, higher scaling of  $V_{LAP}$  increases the magnitude of the Theil–Sen exponents while preserving their sign (negative for heliocentric and positive for cometocentric), with a stronger effect for heliocentric distance. Thus, the trends with heliocentric and cometocentric distances are robust and, particularly for temperature, not very affected by the fraction of spacecraft potential measured.

## 5 DISCUSSION

As stated previously, all data used in this study were selected based on the average cometary ion density being at least 15 per cent that of the LAP/MIP electron density. However, while this is true for the 12 h averages, it does vary on a scan-to-scan basis and helps to illuminate one possible reason ICA densities are generally lower than LAP densities. In some ICA scans, the low energy Maxwellian disappears and the distribution function overall has much lower amplitude. As the ICA density is the integral of the measured distribution function, this subsequently drops as well. Thus, when ICA densities are much lower than LAP/MIP densities, it would seem ICA is not detecting the low energy cometary ions. Likely, this is at least partially due to a field-of-view effect, as the spacecraft potential severely distorts the trajectories of the low energy ions. Near perihelion counterstreaming cold cometary ions were observed in the region of the diamagnetic cavity (Bergman et al. 2021b), indicating that it is indeed possible for multiple cold ion beams to exist, which may not all be in the ICA field-of-view. Because of the trajectory distortion from the spacecraft potential, the field-of-view is increased, although

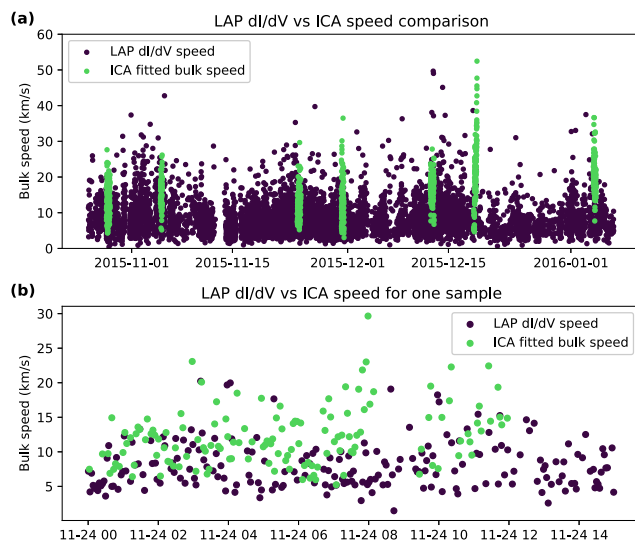


**Figure 10.** The LAP dI/dV effective ion flow speed in purple compared to the results from this study in green. Panel (a) shows data for two months that contain multiple fitted sample periods, while panel (b) shows a zoom in on one of the samples, 2015 November 24. The ICA fitted drift energy has been converted to bulk speed in  $\text{km s}^{-1}$ .

directional information is no longer accurate. It is therefore possible that scans with a relatively complete energy distribution include ions that would normally not be detected by the instrument, allowing us to make a better assessment of the plasma properties. We show some examples of the LAP effective ion flow speeds, derived from dI/dV for each bias voltage sweep, compared to the  $E_i$  from the fitted ICA data in Fig. 10. The ICA fitted drift energy has been converted to bulk speed assuming a particle mass of 19 amu, consistent with the LAP data set. The LAP effective ion flow speed data were taken from the analysed sweep (ASW) data in Eriksson et al. (2020), filtered for quality values (a measure that depends on the goodness of the fit on the ion current slope and the MIP spectrum quality) above 0.7. The figure shows that the LAP and ICA derived speeds generally overlap, although they are not typically the exact same. In many individual samples, such as that in Fig. 10(b), they also show similar trends in time. Comparison of the fitted drift energies with the LAP ion speeds shows generally good agreement to within 1–2 sigma of each other, indicating ICA is likely measuring the majority of the plasma. However, it should be noted that despite the consistency of the ICA and LAP–MIP data, drift energies in this study are generally higher than previously reported LAP values of 2–8  $\text{km s}^{-1}$  in Vigren et al. (2017), approximately 0.4–6 eV for  $\text{H}_3\text{O}^+$ , and on the higher end of flow speeds reported in Johansson et al. (2021) for these time periods, which ranges from  $\sim 1.5$ –14 eV. It is possible that ICA can only detect the full ion distribution when flow speeds are relatively high, which could explain the difference between the bulk speeds found here and in previous studies. Despite this caveat, the LAP–MIP comparison indicates that the ion distribution data used in this work are reasonably complete and useful for scientific interpretation.

As shown in Section 4.3, it is likely that both heliocentric and cometocentric distance are contributors to the changes in drift energy and temperature. Certainly, a larger cometocentric distance can contribute to the increase in E and T close to perihelion for several reasons. For example, at farther cometocentric distances, the same instrument field of view covers a wider spatial area with significant ion production. Thus, ICA will observe ions produced at different

distances that have experienced differing amounts of acceleration. In general, the longer ion travel time from the ionization point to the spacecraft at large cometocentric distances allows for more processes to affect the plasma, many of which will increase either the drift energy or temperature. These processes are also correlated with cometary activity, as the comet ionosphere is larger and more fully developed close to perihelion, regardless of the spacecraft cometocentric distance. The larger exponents for the energy and temperature trends with heliocentric distance suggest that cometary activity and scale size are more important than strictly distance from the comet. Here, we focus on electric fields and wave activity as drivers of the increase in drift energy and temperature.

As explained in the introduction, the comet plasma environment is largely governed by three different electric fields, in order of increasing distance from the comet: the ambipolar field, the polarization electric field, and finally the solar wind convective electric field. The ambipolar field, with its magnitude of  $\sim 1/r_{\text{com}}$ , may be one reason the mean drift energy is higher closer to perihelion when both the comet atmosphere size and spacecraft distance from the nucleus increase. However, effects from all three of these fields can be observed in the ion energy spectra. Although flow direction is not shown here, the additional higher energy ion populations seen in panels (a) and (b) of Fig. 4 have a strong antisunward velocity component, indicating acceleration by the polarization or solar wind electric fields. The second Maxwellian peak is likely ions born farther from the spacecraft that have been accelerated by the polarization electric field or begun the pickup process. Likewise, the high-energy ions have been seen as a signature of pickup ion detection (Broiles et al. 2015; Coates et al. 2015; Behar et al. 2016; Nicolaou et al. 2017; Berčić et al. 2018; Williamson et al. 2022; Moeslinger et al. 2023a), with the highest energy ions likely coming from far upstream of the spacecraft. This mixed population is thus even farther from thermal equilibrium than the original radially expanding ions and so the distribution evolves from the drifting Maxwell–Boltzmann to a more kappa-like distribution. Thus, from the bottom to the top of Fig. 4 (i.e. decreasing heliocentric distance), we see the evolution of the ion spectra away from equilibrium, although the cold, unaccelerated Maxwellian population of ions born close to the spacecraft remains. This results in the fitted drift energy changing very little with cometocentric distance, with  $E \propto r^{0.05}$ . However, the addition of ions born increasingly far away and accelerated to the location of the spacecraft will broaden the spectra, leading to an increase in temperature for high- cometocentric/low-heliocentric distances.

Waves also cannot be ignored as a cause for the inverse correlation with heliocentric distance. Indeed, the presence of a Maxwell–Boltzmann distribution itself is indication of wave activity, as the ions are born with the temperature of the neutral gas, with a distribution function that then evolves towards a Maxwellian as it expands (see e.g. fig. 5 in Vigren & Eriksson 2017). Many types of plasma waves were observed at comet 67P by *Rosetta*, including lower hybrid waves at low-cometocentric distances (André et al. 2017; Karlsson et al. 2017; Stenberg Wieser et al. 2017), singing comet waves generated by pickup ions (Goetz, Plaschke & Taylor 2020), ion acoustic waves (Gunell et al. 2017a,b), possible ion Bernstein waves (Odelstad et al. 2020), and mirror mode waves (Volwerk et al. 2016; Tello Fallau et al. 2023). A larger comet ionosphere with more magnetic pileup and longer travel distance to the spacecraft gives a higher likelihood that the ions measured by ICA have experienced wave–particle interactions. Thus, wave heating is one possible reason for higher temperatures at lower heliocentric distances. Energy transfer from wave–particle interaction could also be responsible for the increase

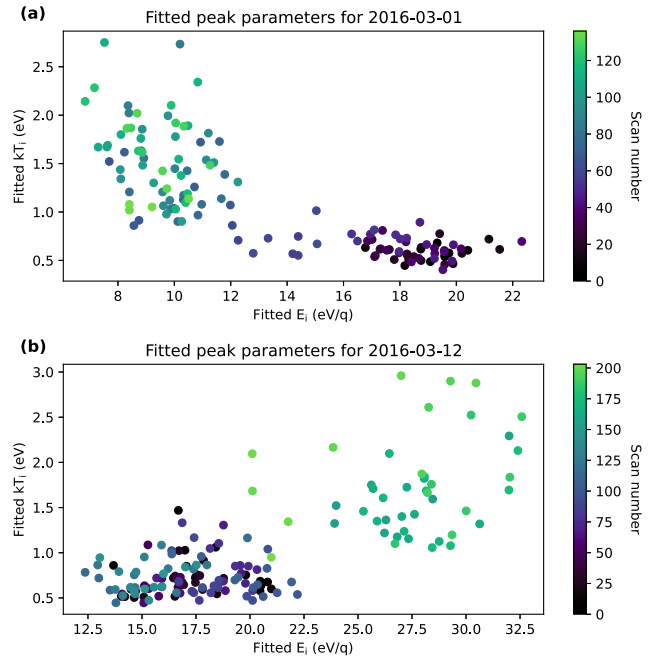


**Figure 11.** The fit parameters for two individual samples on 2016 March 1 (a) and 2016 March 12 (b), with energy on the  $x$ -axis and temperature on the  $y$ -axis. Colour indicates scan number within the sample.

of drift energy approaching perihelion. For one example, large-amplitude steepened magnetosonic waves were observed to be more common at higher outgassing rates near perihelion (Ostaszewski et al. 2021). Such waves occur over much shorter times than the normal ICA 192 s time resolution used here, and indeed their effects can be seen in high time resolution ICA data, with scan times of 4 s (Stenberg Wieser et al. 2017). Because of the fast time-scale for wave activity compared to the time resolution of the data used for this study, it is also a logical reason for the large scan-to-scan variability in both energy and temperature. This is the case throughout all the data, as seen in Fig. 8, but is more prominent closer to perihelion. In general, the comet ionosphere has the highest energy input close to perihelion, as reflected in the increase of cometary ion momentum flux seen in Williamson et al. (2020), and consequently the largest and most complex structure. This then is plausibly the reason for both the larger interquartile range and higher values for  $E$  and  $T$  close to perihelion.

It can be seen in panel (c) of Fig. 8 that, while the majority of the samples have a negative correlation between  $E$  and  $T$ , this is not consistent, and shows no trend with heliocentric distance. For some samples, indicated by the gray dots in the bottom panel of the figure, there is no statistically significant correlation at all. As with the high variability, this is likely due to the transient and dynamic nature of the comet ionosphere. When examining  $E$  versus  $T$  for individual samples, some cases show a clear shift in time over the hours of the sample period, moving from e.g. a cluster of scans with relatively low  $T$  and high  $E$  to later scans with higher  $T$  and lower  $E$  or vice versa. Two such samples are shown in Fig. 11. Panel (a) shows a shift from a negatively correlated cluster with high  $E$  and low  $T$  to a second, strongly negatively correlated sample with low  $E$  and high  $T$ . Another such shift in time, shown in panel (b), occurs for the most positively correlated sample seen in Fig. 8(c), with  $E$  and  $T$  both being originally low, then suddenly increasing, where they remain high for the rest of the time period. The cluster of data points from

the beginning of the sample is only weakly positively correlated, but both a stronger correlation in the second cluster of data points and the shift to higher E and T create a strong positive correlation for the whole sample. Thus, this shifting in time can affect the correlation for a single sample, meaning that the changing plasma conditions also affect the correlation between E and T. Such a change is a clear indication of an event occurring, although whether this is due to a change in the upstream solar wind or a more localized event is not possible to determine from the data. This highlights how dynamic the plasma environment of comet 67P could be and, hence, the need for a statistical approach to understand it.

## 6 CONCLUSIONS

We fit more than 3500 ion energy distributions measured by the ICA instrument with a drifting Maxwell–Boltzmann function. By correcting for spacecraft potential and only choosing time periods with plasma densities comparable to other instruments, we are able to focus on the low-energy cometary ions that would otherwise be difficult to analyse. By doing so, we see that the drift energy and temperature are generally within a relatively narrow range of 11–18 eV and 0.5–1 eV, respectively, for much of the *Rosetta* mission. This is despite large changes in the comet ionosphere during the time periods analysed, such as the formation of the solar wind ion cavity. The drift energy (equivalent to flow speed) is somewhat higher than the mission-wide medians reported from the *Rosetta* LAP data (Johansson et al. 2021); this may be due to selection bias, as the flow may need to be higher energy in order to be observed in full by ICA. However, for the scans analysed, the fitted drift energy is consistent with the coinciding LAP data.

While the drift energy and temperature do not change drastically throughout our samples despite a wide spread, we do see two statistically significant changes: both energy and temperature decrease with increasing heliocentric distance, as does the interquartile range or scan-to-scan variability. This can largely be attributed to the comet ionosphere being both larger in size and more complex at the lowest heliocentric distance, although whether the correlations are strictly due to heliocentric distance or spacecraft distance from the comet, which increased towards perihelion, cannot be determined. We attribute the higher energy and temperature to both the accelerating electric fields and wave–particle interactions, which have more opportunities to accelerate or heat the ions at low heliocentric/large spacecraft distances. As the comet ionosphere increases in complexity, we can observe an evolution of the cometary ion distribution from a single cold Maxwellian population to include higher energy accelerated pickup ions.

## ACKNOWLEDGEMENTS

The work of HW and AJ was supported by Swedish National Space Agency grant 2021–000105. AM was supported by SNSA grant 132/19. The authors thank the members of the *Rosetta* Plasma Consortium team for their helpful discussions.

## DATA AVAILABILITY

The *Rosetta* RPC–ICA, RPC–LAP, and RPC–MIP data are publicly available through the ESA Planetary Science Archives at <https://psa.esa.int/>, with specific data sets cited. Fit parameters for all samples used in the paper are available at <https://data.irf.se/data/williamson2024mnras/>. Mann–Kendall tests were performed with the (0:sc) `pymanckendall`(/0:sc) software package (Hussain & Mahmud 2019).

SCIPY v1.12.0 was used for Theil–Sen regression (Virtanen et al. 2020). Colourmaps were used courtesy of *CMasher* (van der Velden 2020).

## REFERENCES

- André M. et al., 2017, *MNRAS*, 469, S29  
 Behar E., Nilsson H., Wieser G. S., Nemeth Z., Broiles T. W., Richter I., 2016, *Geophys. Res. Lett.*, 43, 1411  
 Bergman S., Stenberg Wieser G., Wieser M., Johansson F. L., Eriksson A., 2020a, *J. Geophys. Res.: Space Phys.*, 125, e27478  
 Bergman S., Stenberg Wieser G., Wieser M., Johansson F. L., Eriksson A., 2020b, *J. Geophys. Res.: Space Phys.*, 125, e27870  
 Bergman S. et al., 2021a, *MNRAS*, 503, 2733  
 Bergman S., Wieser G. S., Wieser M., Nilsson H., Vigren E., Beth A., Masunaga K., Eriksson A., 2021b, *MNRAS*, 14, 1  
 Berčić L., Behar E., Nilsson H., Nicolaou G., Stenberg Wieser G., Wieser M., Goetz C., 2018, *A&A*, 613, 1  
 Brandt J., Faruqhar R., Maran S., Niedner M., von Roseninge T., 1985, in Carusi A., Valsecchi G. eds, *IAU Colloq. 83: Dynamics of Comets: Their Origin and Evolution*. Vol. 115, Springer, Dordrecht, p. 405  
 8-94-009-5400-7.35" skip="true" objectname="ObjectProperty"?)  
 Broiles T. W. et al., 2015, *A&A*, 583, A21  
 Bucciantini L., Henri P., Wattiaux G., Lavorenti F., Dazzi P., Vallières X., 2023, *J. Geophys. Res. (Space Phys.)*, 128, e2023JA031534  
 Carr C. et al., 2007, *Space Sci. Rev.*, 128, 629  
 Coates A. J., 2004, *Adv. Space Res.*, 33, 1977  
 Coates A. J., Burch J. L., Goldstein R., Nilsson H., Wieser G. S., Behar E., 2015, *J. Phys.: Conf. Ser.*, 642, 012005  
 Deca J., Henri P., Divin A., Eriksson A., Galand M., Beth A., Ostaszewski K., Horányi M., 2019, *Phys. Rev. Lett.*, 123, 55101  
 Edberg N. J. et al., 2015, *Geophys. Res. Lett.*, 42, 4263  
 Eriksson A. I. et al., 2007, *Space Sci. Rev.*, 128, 729  
 Eriksson A., Gill R., Johansson E. P., Johansson F. L., 2020, *Rosetta RPC-LAP archive of derived plasma parameters from the COMET ESCORT 4 mission phase, RO-C-RPCLAP-5-ESC4-DERIV2-V1.0*. European Space Agency, <https://archives.esac.esa.int/psa/ftp//INTERNATIONAL-ROS-ETTA-MISSION/RPCLAP/RO-C-RPCLAP-5-ESC4-DERIV2-V1.0>  
 Gilbert R. O., 1987, Technical Report PNL-4660, Statistical Methods for Environmental Pollution Monitoring, Pacific Northwest National Lab. (PNNL), Richland, WA (United States), <https://www.osti.gov/biblio/7037501>  
 Goetz C. et al., 2016a, *MNRAS*, 462, S459  
 Goetz C. et al., 2016b, *A&A*, 588, 1  
 Goetz C., Plaschke F., Taylor M. G. G. T., 2020, *Geophys. Res. Lett.*, 47, e2020GL087418  
 Grensemann M. G., Schwemh G., 1993, *J. Geophys. Res.*, 98, 20907  
 Gringauz K. I. et al., 1986, *Nature*, 321  
 Gunell H. et al., 2017a, *MNRAS*, 469, S84  
 Gunell H. et al., 2017b, *A&A*, 600, 1  
 Hussain M. M., Mahmud I., 2019, *J. Open Source Softw.*, 4, 1556  
 Johansson F. L., Eriksson A. I., Gilet N., Henri P., Wattiaux G., Taylor M. G. G. T., Imhof C., Cipriani F., 2020, *A&A*, 642, A43  
 Johansson F. L. et al., 2021, *A&A*, 653, A128  
 Karlsson T. et al., 2017, *Geophys. Res. Lett.*, 44, 1641  
 Kendall M. G., 1975, Rank correlation methods, 4th, 2d impression, edn. Griffin London, London, p. 1  
 Legates D. R., McCabe G. J., Jr, 1999, *Water Resour. Res.*, 35, 233  
 Mandt K. E. et al., 2016, *MNRAS*, 462, S9  
 Mann H. B., 1945, *Econometrica*, 13, 245  
 Masunaga K., Nilsson H., Behar E., Stenberg Wieser G., Wieser M., Goetz C., 2019, *A&A*, 630, A43  
 Moeslinger A., Nilsson H., Stenberg Wieser G., Gunell H., Goetz C., 2023a, *J. Geophys. Res.: Space Phys.*, 128, e2023JA031746  
 Moeslinger A., Wieser G. S., Nilsson H., Gunell H., Williamson H. N., LLera K., Odelstad E., Richter I., 2023b, *J. Geophys. Res.: Space Phys.*, 128, e2022JA031082

- Nicolaou G., Behar E., Nilsson H., Wieser M., Yamauchi M., Berčić L., Wieser G. S., 2017, *MNRAS*, 469, S339
- Nilsson H., 2021a, ROSETTA-ORBITER 67P RPCICA 4 EXT3 RESAMPLED AND CALIBRATED V1.0, RO-C-RPCICA-4-EXT3-PHYS-MASS-V1.0. European Space Agency. <https://pdssbn.astro.umd.edu/holdings/ro-c-rpcica-4-ext3-phys-mass-v1.0/dataset.shtml>
- Nilsson H., 2021b, Technical Report 1.5, RPC-ICA User Guide. IRF, Kiruna
- Nilsson H. et al., 2007, *Space Sci. Rev.*, 128, 671
- Nilsson H. et al., 2015, *A&A*, 581, 1
- Nilsson H. et al., 2017, *MNRAS*, 469, S252
- Nilsson H. et al., 2018, *A&A*, 616, 1
- Odelstad E. et al., 2015, *Geophys. Res. Lett.*, 42, 10126
- Odelstad E., Stenberg-Wieser G., Wieser M., Eriksson A. I., Nilsson H., Johansson F. L., 2017, *MNRAS*, 469, S568
- Odelstad E. et al., 2020, *J. Geophys. Res.: Space Phys.*, 125, 1
- Ostaszewski K. et al., 2021, *Ann. Geophys.*, 39, 721
- Poh G. et al., 2021, *J. Geophys. Res.: Space Phys.*, 126, e29224
- Ruhunusiri S. et al., 2016, *Geophys. Res. Lett.*, 43, 4763
- Sen P. K., 1968, *J. Am. Stat. Assoc.*, 63, 1379
- Stenberg Wieser G. et al., 2017, *MNRAS*, 469, S522
- Szegö K. et al., 2000, *Space Sci. Rev.*, 94, 429
- Tello Fallau A., Goetz C., Simon Wedlund C., Volwerk M., Moeslinger A., 2023, *Ann. Geophys.*, 41, 569
- Theil H., 1992, in Raj B., Koerts J., eds, *Henri Theil's Contributions to Economics and Econometrics: Econometric Theory and Methodology*. Springer Netherlands, Dordrecht, p. 345, [https://doi.org/10.1007/978-94-011-2546-8\\_20](https://doi.org/10.1007/978-94-011-2546-8_20)
- Troignon J. G. et al., 2007, *Space Sci. Rev.*, 128, 713
- van der Velden E., 2020, *J. Open Source Softw.*, 5, 2004
- Vigren E., Eriksson A. I., 2017, *AJ*, 153, 150
- Vigren E. et al., 2017, *MNRAS*, 469, S142
- Virtanen P. et al., 2020, *Nat. Methods*, 17, 261
- Volwerk M. et al., 2016, *Ann. Geophys.*, 34, 1
- Wattiaux G., Henri P., Gilet N., Vallières X., Deca J., 2020, *A&A*, 638, A124
- Williamson H. N., Nilsson H., Stenberg Wieser G., Eriksson A. I., Richter I., Goetz C., 2020, *Geophys. Res. Lett.*, 47, e88666
- Williamson H. N., Nilsson H., Stenberg Wieser G., Moeslinger A., Goetz C., 2022, *A&A*, 660, A103
- Wolff R. S., Goldstein B. E., Yeates C. M., 1980, *J. Geophys. Res.: Space Phys.*, 85, 7697

This paper has been typeset from a  $\text{\TeX}/\text{\LaTeX}$  file prepared by the author.